MSDE

PAPER

View Article Online
View Journal | View Issue

Cite this: *Mol. Syst. Des. Eng.*, 2021, 6, 903

Alkylation of poly-substituted aromatics to probe effects of mesopores in hierarchical zeolites with differing frameworks and crystal sizes†

Hayat I. Adawi, Florence O. Odigie and Michele L. Sarazen *

This study examines how the inherent diffusion constraints of MFI (3D, pore-limiting diameter (PLD) = 0.45 nm), BEA (3D, PLD = 0.60 nm), and MOR (1D, PLD = 0.65 nm) zeolite architectures, at both nanocrystal (nMFI, nBEA, nMOR; $d_{crystal} < 0.5$ μm) and microcrystal (μBEA, μMOR; $d_{crystal} > 0.5$ μm) scales, impact functions of mesopores in their hierarchical analogs. Reactivities, deactivation rates, and product selectivities were compared among zeolites, as well as to a mesoporous aluminosilicate control (Al-MCM-41; PLD = 6.2 nm), during Friedel–Crafts alkylation of 1,3,5-trimethylbenzene (TMB; d_{vdW} = 0.72 nm) with benzyl alcohol (BA; d_{vdW} = 0.58 nm) to form 1,3,5-trimethyl-2-benzylbenzene (TM2B; d_{vdW} = 0.75 nm). Operation in the neat liquid phase ($[TMB]_0 : [BA]_0$ = 35 : 1, 393 K) ensured that the parallel BA self-etherification to yield dibenzyl ether (DBE; d_{vdW} = 0.58 nm) occurred only at the expense of TM2B production when the alkylation reaction was impeded due to hindered access of TMB to confined protons. Investigation of secondary TM2B formation from reaction of DBE with TMB at low [BA]/[DBE] indicates an additional route of selectivity control for hierarchical zeolites that can achieve high BA conversion ($X_{BA} > 0.9$) with no DBE cofeed. These findings highlight a compounding advantage of increased diffusivity in mesopores that alter rates, extend lifetimes, and subsequently permit secondary reactions that enable significant shifts in product distribution. Fundamental insights into hierarchical zeolite reaction–diffusion–deactivation for alkylation of poly-substituted aromatics, as detailed here, can be applied broadly to reactions of other bulky species, including biomass-derived oxygenates, for more atom-efficient chemical and fuel production.

Received 30th May 2021,
Accepted 27th July 2021

DOI: 10.1039/d1me00062d

rsc.li/molecular-engineering

Design, System, Application

The molecular design strategy employed here involves facile restructuring of the internal porous architecture of conventional, microporous zeolites *via* post-synthetic acid and/or base treatments to introduce auxiliary mesopores with optimized diffusion capabilities, which ultimately impact catalytic rates, selectivities, and lifetimes. Intended functionalities of the hybrid, hierarchical zeolite systems include improved accessibility of viable catalytic active sites to reaction moieties, thereby enabling reaction pathways otherwise excluded from prohibitively narrow micropores. A significant constraint on designing these hierarchical zeolites is the requirement for facile, scalable synthesis, such as *via* post-synthetic leaching with mild base utilized here. Combined synthetic, kinetics, and computational results from our presented findings yield fundamental insight into zeolite structure–function relations that apply broadly to other zeolite-catalyzed processes for more efficient chemical and fuel production.

1 Introduction

Upgrading bulky biomass- and petroleum-derived platform molecules, including poly-substituted aromatics, encounters exceptional diffusional challenges in zeolite catalysts. These challenges limit the ability of shape- and size-selective micropores (pore-limiting diameter (PLD) < 2 nm) within zeolites to exercise high degrees of control over product distributions through preferential van der Waals solvation of reaction moieties with sizes approaching void diameters.[1–5] For example, in zeolite-catalyzed alkylation of aromatics, especially in the liquid phase, diffusivities are reduced to extremes that result in premature deactivation through fouling by polycyclic aromatics, low selectivity to desired bulky products, and/or low lifetime conversions.[6–9] Two-dimensional zeolites, including delaminated and pillared zeolites, significantly increase diffusivities at the expense of (hydro)thermal stability and/or facile synthesis.[10–12] Ordered

Department of Chemical and Biological Engineering, Princeton University, New Jersey, USA. E-mail: msarazen@princeton.edu

† Electronic supplementary information (ESI) available. See DOI: 10.1039/d1me00062d

mesoporous aluminosilicates, such as Al-MCM-41 or Al-SBA-15,[13,14] lack hydrothermal stability and/or cannot selectively solvate reaction moieties within voids much larger than molecular dimensions.[12,15,16] Hierarchical zeolites containing auxiliary mesopores (PLD = 2–50 nm) give higher lifetime conversions, mitigate fouling, and tolerate the severe thermal recycling treatments (>823 K) that are often necessary to remove carbonaceous deposits.[7,17–20] Here, we demonstrate how complex reaction networks involving multiple side reactions can be deductively tied to structure–function relations of mesopores in hierarchical zeolites, including how mesopores can lower deactivation rates and direct competitive reaction mechanisms in ways that require more detailed quantification than through typical bulk descriptors like maximum conversion and gross product yields.

This study examines how the inherent diffusion constraints of purely microporous MFI, BEA, and MOR zeolites that arise from framework architecture and crystal size (nanocrystals, $d_{crystal} < 0.5$ μm; microcrystals, $d_{crystal} > 0.5$ μm) impact the efficacy of mesopores in their hierarchical analogs (MFI-h, BEA-h, MOR-h). The ability of these samples to mitigate deactivation and control product selectivity is further compared to an Al-MCM-41 control during the probe liquid-phase alkylation of 1,3,5-trimethylbenzene (TMB) with benzyl alcohol (BA) to form 1,3,5-trimethyl-2-benzylbenzene (TM2B). This probe reaction occurs in parallel with self-etherification of BA to form dibenzyl ether (DBE) (Fig. 1), enabling consideration of diffusion extremes to yield fundamental insights into structure–function relations of hierarchical zeolites that are owed rigorous investigation. Previous studies reported that 10-membered ring (10-MR) MFI micropores were prohibitively narrow for TMB alkylation, which occurred exclusively on surface protons of MFI or on external protons in the silica-pillared or self-pillared pentasil analogs of MFI.[11,21] Increasing MFI crystal size reduced TMB alkylation and BA self-etherification rates in spite of higher external surface areas of larger crystals, because the larger crystals had fewer external protons, as evidenced by quantification during ethanol dehydration on microporous MFI titrated with 2,6-di-*tert*-butylpyridine and pyridine.[10,22] However, corresponding reaction models did not include deactivation rate constants, even for 17 μm MFI crystals with high Thiele moduli ($\phi \sim 1000$; eqn (1)), partially due to differential conversion employed through low (343 K) reaction temperatures.[10,22] Similarly, mesopore effects on deactivation rates were not considered on hierarchical BEA, where TMB alkylation reportedly occurred more readily in its 12-MR channels than within the 10-MR channels of MFI.[23] While total BA conversion and TM2B selectivity for a given reaction time increased for hierarchical BEA (BEA-h) prepared through post-synthetic basic recrystallization of BEA, reaction–diffusion relationships, as quantified by the Thiele modulus, have not been probed for BEA systems.[23] The ability of mesopores to facilitate access to internal protons depends on proton siting within hierarchical structures and mesopore–micropore connectivity.[24] Such outcomes confirm that mesopore efficacy for an *n*th order reaction is partly contextualized by the Thiele modulus (presented here for a spherical catalyst pellet):

$$\phi_{n,A}{}^2 = \frac{k_n \rho_{H^+} [A]^{n-1}}{9 D_e / R^2} \quad (1)$$

where D_e is effective diffusivity, R is crystal radius, k_n is the proton-normalized rate constant of microporous zeolites, ρ_{H^+} is volumetric zeolite proton density, and [A] is reactant concentration.

Along with utilizing the difference in size of moieties involved in the primary alkylation pathway compared to the primary etherification pathway to probe interconnectivity of micro- and mesopores, we consider the formation of TM2B from DBE and TMB, a secondary pathway occurring at low [BA]/[DBE] that has been overlooked or de-emphasized by previous studies. Studies comparing MFI with its pillared analogs were intentionally operated at low temperatures (343 K), to prevent this secondary reaction by maintaining BA conversions below 10%,[11,21,22] and studies of BEA and BEA-h did not report secondary TM2B formation, likely due to high [BA]/[DBE] for observed reaction times,[23] in agreement with our findings. Here, we report significant secondary DBE consumption on Al-MCM-41 and nanocrystalline MOR-h (nMOR-h). To our knowledge, no MOR derivative has yet been thoroughly examined for this reaction system, implying that comprehensive, comparative studies of microporous architecture effects are needed. We show that the inaccessibility to protons within 8-MR MOR pockets relegates alkylation of poly-substituted aromatics like TMB to surface protons and larger 12-MR channels, the latter of which contain fewer than 50% of total active sites.[21,25] The presented work also deconvolutes the nuanced effects of channel dimensionality by comparing systems of differing dimensionality with similar pore sizes (1D, 12-MR MOR v. 3D, 12-MR BEA) as well as systems of differing pore sizes with similar dimensionality (10-MR, 3D MFI v. 12-MR, 3D BEA) in hierarchical analogs. Further, our study shows that

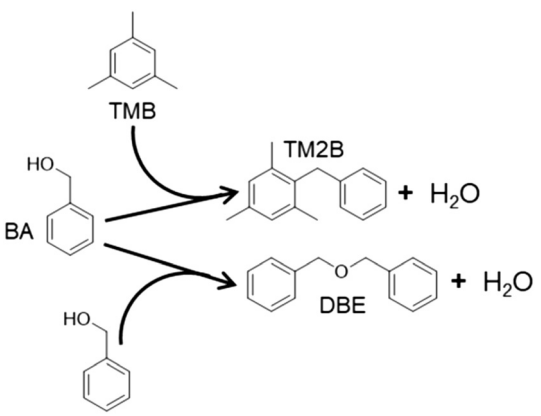

Fig. 1 Acid-catalyzed parallel TMB alkylation and BA self-etherification reactions to yield TM2B and DBE.

experimentally observed fouling of microporous zeolites manifests in quantifiable and significant deactivation rates that decline with increasing mesoporosity.

Our findings indicate that the extent to which post-synthetically induced mesoporosity in zeolites reduces deactivation rates and enhances selectivity to bulky reaction products in complex reaction networks strongly depends on the inherent diffusional constraints presented by microporous architectures and crystal sizes. Our work expands the suite of zeolite frameworks studied thus far to include a more comprehensive representation of pore architectures, and we build a complex reaction model that includes effects of deactivation and secondary reactions. Deduction of structure–function effects for this probe alkylation reaction enables consideration of diffusion extremes, involving combination reactions for poly-substituted aromatics in the liquid phase, to understand the maximum potential of mesopores to successfully shift zeolite operation from diffusion-limited to kinetically controlled regimes.

2 Experimental methods

2.1 Synthesis of parent catalysts

Published methods were adapted (section S.1†) to synthesize all MFI,[26,27] BEA,[28–32] MOR,[33] and Al-MCM-41.[34] nMOR was procured commercially (CBV 21A, Si/Al = 10, Zeolyst). In a typical synthesis, an aqueous solution of NaOH (98.7%, Fisher Scientific) and/or $NaAlO_2$ (50–56 wt% Al_2O_3, 37–45% Na_2O, Sigma-Aldrich) was added dropwise while stirring to an SiO_2 gel containing structure-directing agents (SDA) such as quaternary ammonium hydroxides and/or inorganic salts.[35] The gel was then crystallized in a PTFE-lined, stainless steel autoclave or a high-density polyethylene bottle filled to 1/3 capacity for 15–168 h at 373–443 K to yield white solids. Solids were collected and washed repeatedly with deionized H_2O *via* centrifugation (7200 × *g*, 10 min cycles) or vacuum filtration until supernatant pH ≤ 9, and then dried overnight at 343–373 K to yield the Na^+-analog of the parent catalyst (Na-nMFI, Na-nBEA, Na-μBEA, Na-nMOR, Na-μMOR, Na–Al-MCM-41). For methods employing an organic SDA, the dried catalyst was then calcined at 823 K overnight under 150 sccm air zero (Airgas) by first ramping to 653 K at 7.5 K min^{-1}, then to 823 K at 0.8 K min^{-1}.

All Na^+-analogs of catalysts were thrice ion-exchanged by dispersion in aqueous NH_4NO_3 (99.8%, Fisher Scientific) at concentrations such that $[NH_4^+]:[Na^+] \geq 50$ (0.5–2 M NH_4NO_3) while stirring for 3 h in an oil bath at 353 K, followed by centrifugation (7200 × *g*, 10 min) and redispersion in fresh NH_4NO_3 solution.[36] After the third cycle, catalysts were collected and washed copiously with deionized H_2O *via* centrifugation. NH_4^+-Analogs of catalysts were calcined for 6 h at 823 K under 150 sccm air zero to yield their catalytically active, proton analogs by first ramping to 653 K at 7.5 K min^{-1}, then to 823 K at 0.8 K min^{-1}. Proton analogs of catalysts are denoted without a hyphenated ion prefix (nMFI, nBEA, μBEA, nMOR, μMOR, Al-MCM-41).

2.2 Synthesis of hierarchical zeolites

Hierarchical analogs of MFI, BEA, and MOR were prepared by post-synthetic modification of parent zeolites in their proton forms.

nBEA-h and μBEA-h were prepared *via* basic recrystallization by suspending nBEA or μBEA in 0.2 M NaOH (27 mL g^{-1} BEA) in a PTFE-lined, stainless steel autoclave (45 mL capacity only) and heating statically for 21 h at 423 K.[23] Samples were collected and washed repeatedly *via* centrifugation (7200 × *g*, 10 min) in deionized H_2O until supernatant pH ≤ 9, then dried overnight at 343 K to yield Na-nBEA-h and Na-μBEA-h.

nMFI-h was prepared by conventional desilication.[37–39] nMFI was suspended in 0.2 M NaOH (30.3 mL g^{-1} nMFI) with stirring in an HDPE bottle in an oil bath at 338 K for 30 min or 15 min to yield Na-nMFI-h1 or Na-nMFI-h2, respectively.[40] Samples were immediately quenched with ice water, then collected and washed repeatedly *via* centrifugation (7200 × *g*, 10 min) with deionized H_2O until supernatant pH ≤ 9. Samples were dried overnight at 343 K.

nMOR-h and μMOR-h were prepared by dealumination in aqueous HNO_3 (diluted from 69.3%, Fisher Scientific) followed by conventional desilication.[41–44] nMOR and μMOR were refluxed in an oil bath at 373 K under magnetic stirring in 2 M HNO_3 for 4 h (for nMOR-h) or 6 M HNO_3 for 2 h (for μMOR-h). Samples were immediately quenched with ice water, collected and washed repeatedly *via* centrifugation (7200 × *g*, 10 min) with deionized H_2O until pH = 7, and then dried overnight at 343 K. Dealuminated MOR was then calcined for 2 h at 823 K under 150 sccm air zero. After calcination, dealuminated nMOR or μMOR was suspended in 0.2 M NaOH (30.3 mL g^{-1} MOR) with stirring in an HDPE bottle in an oil bath at 338 K for 30 min. Desilicated MOR was immediately quenched with ice water, then collected and washed repeatedly *via* centrifugation (7200 × *g*, 10 min) with deionized H_2O until supernatant pH ≤ 9. Samples were dried overnight at 343 K to yield Na-nMOR-h and Na-μMOR-h.

As with Na^+-analogs of microporous zeolites, Na^+-analogs of hierarchical zeolites were ion-exchanged with aqueous NH_4NO_3 and calcined to yield their catalytically active, proton analogs, denoted without hyphenated ion prefixes (*i.e.*, nMFI-h1, nMFI-h2, nBEA-h, μBEA-h, nMOR-h, μMOR-h).

2.3 Characterization of catalysts

Crystal structures were confirmed by powder x-ray diffraction (XRD; Bruker D8 Discover diffractometer; 0.154 nm Cu Kα radiation) of zeolite samples mounted on glass slides with a thin layer of vacuum grease. Crystal morphologies and sizes were deduced from scanning electron microscopy (SEM; XL30 FEG-SEM) of zeolites dusted onto studs loaded with carbon tape. Si/Al ratios were measured by energy-dispersive X-ray spectroscopy (EDXS; XL30 FEG-SEM). Brunauer–Emmett–Teller surface areas (S_{BET}) and Brunauer–Joyner–Halenda

(BJH) pore size distributions were calculated for cylindrical pores using N_2 physisorption (Micromeritics 3Flex) isotherms (77 K) of samples degassed overnight (125 Torr at 423 K) on a Schlenk line.[45,46] Proton concentrations were measured by temperature-programmed NH_3 desorption (NH_3-TPD; Micromeritics Autochem II) of samples pretreated with *in situ* heating to 673 K for 60 min under He (30 sccm).

2.4 Friedel–Crafts alkylation of 1,3,5-trimethylbenzene (TMB) with benzyl alcohol (BA)

In a typical batch kinetics experiment, catalyst (0.1 g) was pretreated by heating statically at 523 K for 2 h in an uncapped, two-neck, round-bottom flask to desorb H_2O.[23] After cooling to ambient temperature, the reactor was immediately charged with TMB (9.6 mL, 99%, Acros Organics), connected through one neck to a reflux condenser, and capped at the second neck with a glass stopper. The reactor was held with stirring at 363 K for 1.5 h in an oil bath. The bath was then heated to 393 K, after which BA (0.21 mL, 99.97%, Chem Impex International) was injected to initiate reaction (t = 0 min). Aliquots (t = 2, 10, 20, 30, 45, 80, 120 min) were extracted by a Pasteur pipette through the briefly removed glass stopper, filtered through a cotton-plugged pipette, and immediately refrigerated. These aliquots were sampled (0.2 μL) and diluted in $CDCl_3$ (600 μL, 99.8% atom D, Sigma-Aldrich) for ^{1}H-NMR (500 MHz) utilizing the following chemical shifts BA: δ 4.63 (s, 2H). DBE: δ 4.55 (s, 4H). TM2B: δ 4.30–2.50 (m, 2H).

2.5 Secondary reaction deduction: dibenzyl ether (DBE) cleavage reaction

Catalyst loading and pretreatment followed section 2.4. After cooling to ambient temperature, the reactor was immediately charged with *n*-octane solvent (9.8 mL, >97.0%, Tokyo Chemical Industries), which is inert at our reaction conditions. The reactor was connected through one neck to a reflux condenser, capped at the second neck with a glass stopper, and heated to 393 K with stirring in an oil bath without the 363 K hold as in section 2.4, owing to facile diffusion of *n*-octane in zeolite micropores. At 393 K, DBE (0.04 mL, 98%, Sigma-Aldrich) and H_2O (0.03 mL) were injected to initiate reaction (t = 0 min). Aliquots (t = 2, 7, 15, 30, 60, 90 min) were collected, processed, and analyzed by ^{1}H-NMR.

2.6 Secondary reaction deduction: formation of TM2B from DBE and TMB

Catalyst loading, pretreatment, and TMB loading followed section 2.4. After holding the batch at 363 K for 1.5 h with stirring, DBE (0.04 mL) was injected to initiate reaction (t = 0 min). Aliquots (t = 2, 10, 20, 30, 45, 80, 120 min) were collected, processed, and analyzed by ^{1}H-NMR.

2.7 Titration of nMFI with 2,4,6-trimethylpyridine (TMPy)

The reaction procedure followed section 2.4, except the reactor was first charged with TMPy (0.4 mL, 98%, Oakwood Chemical) to fully saturate the catalyst for 30 s prior to TMB charge.[21]

2.8 Periodic density functional theory (DFT) for probing molecule solvation

The Vienna *ab initio* simulation package (VASP)[47–50] was utilized to optimize structures and extract dispersive energies for gas phase molecules (BA, TMB, DBE, TM2B), bare microporous zeolites (MFI, BEA, and MOR), and adsorbates.[51] Electron core interactions were modeled with projector-augmented wave (PAW) pseudopotentials.[52,53] Exchange and correlation energies were calculated with the revised Perdew–Burke–Ernzerhof (RPBE) functional for gas phase molecules and bare zeolites or the PBE functional for adsorbates.[54–56] Solvated molecules and bare zeolite optimizations also used a 1 × 1 × 1 Monkhorst–Pack *k*-point mesh to sample the first Brillouin zone.[57] All dispersive forces were calculated with DFT-D3 during energy minimization.[58,59]

Free molecules were described by placing them into 2 × 2 × 2 nm^3 cells to prevent neighboring cell interactions. Zeolites were optimized using CIF files[60] as 1 × 1 × 1 characteristic MFI unit cells, 2 × 1 × 2 BEA supercells, or 1 × 1 × 3 MOR supercells containing one proton each at channel intersections (MFI, BEA) or straight channels (MOR) to prevent neighboring cell interactions. Net dispersive energies attributed to host–guest interactions (ΔE_{disp}) were estimated by subtracting total dispersive energies of bare zeolites ($E_{zeolite}$) and gas phase molecules ($E_{molecule}$) from total dispersive energies of adsorbed molecules ($E_{adsorbate}$):

$$\Delta E_{disp} = E_{adsorbate} - (E_{zeolite} + E_{molecule}) \quad (2)$$

3 Results and discussion

3.1 Bulk rate and selectivity descriptors yield insight into solvation effects in microporous zeolites

Temporal concentrations of benzyl alcohol ([BA]), 1,3,5-trimethyl-2-benzene ([TM2B]), and dibenzyl ether ([DBE]) were tracked with ^{1}H-NMR (section 2.4) and used to calculate total BA conversion to both TM2B and DBE (X_{BA}; eqn (3)) and TM2B selectivities (S_{TM2B}; eqn (4)).

$$X_{BA} = \frac{[BA]_0 - [BA]}{[BA]_0} \quad (3)$$

$$S_{TM2B} = \frac{[TM2B]}{[TM2B] + 2[DBE]} \quad (4)$$

S_{TM2B} here is defined as the fractional selectivity of BA to form TM2B over DBE. Discussion of the effects of inherent zeolite microporous architectures on rates and selectivities is first considered within the context of similar crystal sizes

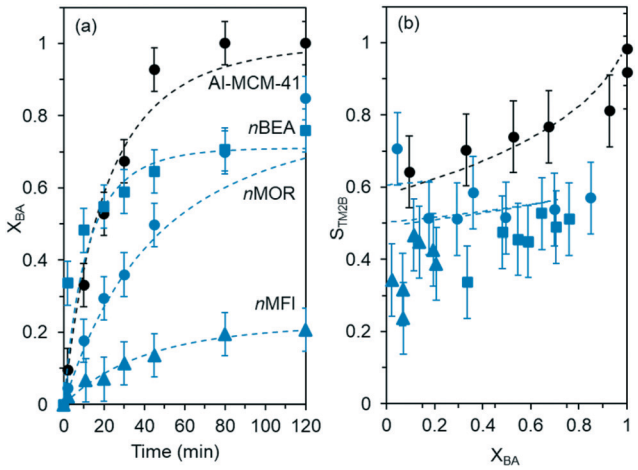

Fig. 2 Fitted temporal (a) X_{BA} (b) and S_{TM2B} for Al-MCM-41 (●), nMOR (●), nBEA (■), and nMFI (▲) (neat, $[TMB]_0:[BA]_0$ = 35 : 1, 393 K). Dashed lines correspond to model fits.

(nMFI, nBEA, nMOR) to preclude artifacts of significantly different diffusion path lengths (Fig. 2); these samples are further compared to the Al-MCM-41 control. The dashed lines shown in Fig. 2 represent fitted models that are described in detail in section 3.3; the bulk descriptors will be first used within the context of guest molecule solvation to give the prerequisite insight for the subsequent analysis.

X_{BA} profiles were interpreted as initial and cumulative total proton-normalized rates of BA consumption (Table 1), the former calculated from the slope of the tangent line to the fitted X_{BA} profile at t = 0 min and the latter calculated from the average consumption of BA over 120 min. The mesoporous Al-MCM-41 gave the highest initial rate (340 mM-BA min^{-1} $mmol\text{-}H^{+-1}$), highest cumulative rate (57 mM-BA min^{-1} $mmol\text{-}H^{+-1}$), and highest S_{TM2B} at all $X_{BA} > 0.1$ (Fig. 2b), consistent with its large mesopores (PLD = 6.2 nm) being able to mitigate significant diffusional limitations.

In contrast, the nMFI (PLD = 0.45 nm) gave the lowest initial rate (20 mM-BA min^{-1} $mmol\text{-}H^{+-1}$) and lowest cumulative rate (6.2 mM-BA min^{-1} $mmol\text{-}H^{+-1}$). nBEA (PLD = 0.60, 3D) gave a higher initial rate than nMOR (PLD = 0.65, 1D), respectively 90 and 60 mM-BA min^{-1} $mmol\text{-}H^{+-1}$, but a lower cumulative rate than nMOR (9.2 and 24 mM-BA min^{-1} $mmol\text{-}H^{+-1}$, respectively). The higher initial rate on nBEA, corresponding to a steeper initial X_{BA} profile, is consistent with enhanced mass transport within the interconnected 3D channeling of the native BEA architecture, in contrast to unidirectional mass transport within the native MOR architecture. It should be noted, though, that conversion on nMOR is still increasing at the end of the two hours, further evidence of why a static conversion data point is an incomplete comparison. Further, the lower cumulative rate on nBEA is consistent with more rapid subsequent deactivation, discussed in section 3.3.

The higher S_{TM2B} for nMOR compared to nBEA at initial data points ($X_{BA} < 0.4$) could suggest different solvation of reaction moieties within channels and voids of varying diameters. Subsequent convergence of S_{TM2B} for nMOR and nBEA at higher X_{BA} (*i.e.*, longer reaction times) is consistent with catalyst deactivation, which partially nullifies marginal solvation differences between nMOR and nBEA because of internal micropore blockage by carbonaceous deposits. Deactivation progresses faster on nBEA than nMOR, as suggested from a conversion profile that plateaus at $X_{BA} \sim 0.7$ for nBEA but does not plateau on nMOR within 2 h of reaction. Increasing S_{TM2B} for nBEA is consistent with rapid deactivation that relegates catalysis to surface or sub-surface protons, which are more accessible to TMB than confined internal protons. Higher S_{TM2B} due to faster deactivation was similarly observed for μMOR than nMOR, as described further in section 3.3.

DFT-calculated van der Waals diameters (d_{vdW}) of reaction moieties were compared to widely reported PLD of zeolite architectures (Fig. 3) to investigate solvation differences.[60] These d_{vdW} are calculated as the shortest cross-sectional ray for a given molecule while incorporating the van der Waals radii of all atoms, resulting in a metric akin to a kinetic

Table 1 Initial and cumulative rates of BA consumption for nanocrystalline, microporous zeolites and Al-MCM-41 normalized by total proton densities. Values in parenthesis are 95% confidence intervals

	Rate[a]	
Catalyst	Initial	Cumulative
Al-MCM-41 ●	340 (1)	57 (3)
nBEA ■	90 (1)	9.2 (1.3)
nMOR ●	60 (1)	24 (7)
nMFI ▲	20 (1)	6.2 (0.3)

[a] [mM-BA min^{-1} $(mmol\text{-}H^{+})^{-1}$].

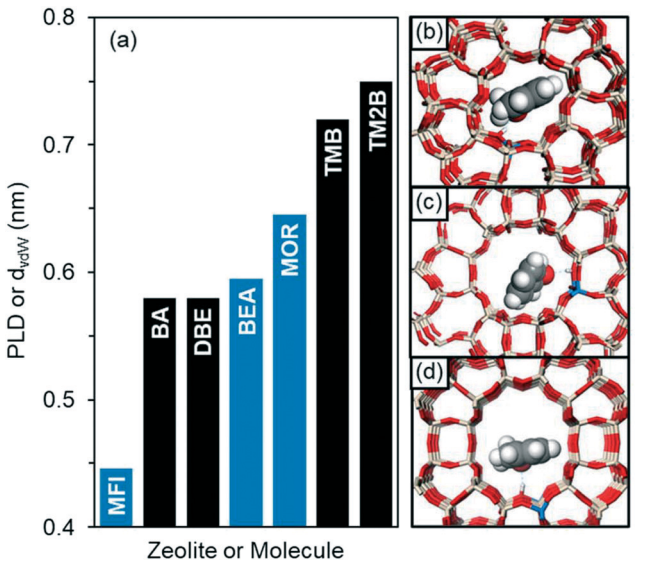

Fig. 3 (a) PLD (nm) of microporous zeolites relative to d_{vdW} (nm) of DFT-optimized molecules, and DFT-optimized structures for BA adsorbed at the proton in (b) MFI, (c) BEA, and (d) MOR with the Al atom in blue.

diameter (Fig. S3†). While d_{vdW} > PLD does not preclude molecule solvation within the zeolite micropore due to inherent flexibility of the aluminosilicate backbone, molecules with sizes approaching void diameters may exhibit constrained diffusion, as confirmed by lower diffusivities of TMB in smaller diameter zeolites.[61–65] MFI straight and sinusoidal channels are significantly smaller than all reaction moieties (Fig. 3a) in agreement with lower reaction rates (Table 1). MOR and BEA have PLDs similar to sizes of reaction moieties, which are expected to allow ingress, albeit with significantly greater diffusion constraints relative to Al-MCM-41, which has mesopores over eight times greater than TM2B (d_{vdW} = 0.75 nm). DFT-calculated structures for adsorbed BA (hydrogen-bound to the proton) in MFI, BEA, and MOR (Fig. 3b–d) yield additional visual and energetic metrics for the impacts of channel size on X_{BA}. The optimized structure of BA (d_{vdW} = 0.58) indicates that BA preferentially sits at intersections of straight and sinusoidal channels that are slightly larger in size but only accessible through narrower pores, which leads to lower diffusivity *via* steric constraints. BEA and MOR impose fewer steric constraints on BA, consistent with higher initial and cumulative rates than on MFI (Table 1).

Changes in dispersive energies relative to the bare zeolites and gas phase molecules (ΔE_{disp}; eqn (2)) calculated for BA, TMB, DBE, and TM2B generally become less negative (*i.e.*, indicative of less stabilization) according to |nMFI| > |nMOR| > |nBEA| (Table 2). Here, the high values for MFI are somewhat misleading as they do not account for activated diffusion of molecules through the pores of smaller dimension, which form undulations along the diffusion pathway that impose a maximum diffusion constraint according to the smallest diameter.[66] Consequently, a snapshot of adsorbed TMB, which reportedly cannot diffuse through 10-MR MFI channels to reach intersecting voids,[10,21,22] but can fit within its intersection, gives a high $|\Delta E_{disp}|$ = 163 kJ mol^{-1}. The ramification of this difference in stabilization, discussed further in section 3.3, is that exclusive alkylation of TMB at surface protons yields surface proton-normalized alkylation rates on nMFI of similar magnitude to those observed on Al-MCM-41 and some hierarchical zeolites. Sterically hindered solvation of other moieties (BA, DBE) within MFI micropores also leads to more rapid deactivation and lower cumulative BA consumption rates on nMFI than nBEA or nMOR.

Additionally, the optimized structures for BA, TMB, and TM2B in BEA also result in molecules stabilized at intersections of 12-MR channels, resulting in less solvated moieties compared to MOR. However, $|\Delta E_{disp}|$ for DBE is similar in BEA (136 kJ mol^{-1}) and in MOR (131 kJ mol^{-1}). The longest end-to-end molecular distance of DBE (1.15 nm, Fig. S3†) causes DBE to preferentially orient parallel to the 12-MR channel in BEA instead of entering an intersecting void (Fig. S4†), which only has a diameter of 0.67 nm.[60] Consequently, the similar $|\Delta E_{disp}|$ in BEA and MOR is consistent with high van der Waals interactions within the slightly narrower pore of BEA (PLD = 0.60 nm, compared to 0.65 nm for MOR). While the end-to-end molecular distance of TM2B (1.00 nm) is similarly greater than the intersecting void diameter of BEA, TM2B also has an 85° bent shape (Fig. S3†) that allows it to saddle the intersecting void of BEA. Additionally, all orientations explored for a given host–guest solvation pair gave similar ΔE_{disp}, including both hydrogen-bound and π-bound BA at protons.

The relatively large diameter of TMB (d_{vdW} = 0.72 nm) reportedly prohibits ingress into MFI altogether, and thus relegates all TMB alkylation exclusively to protons at crystal surfaces and pore mouths.[21] This hypothesis was probed experimentally by repeating alkylation on nMFI after saturation with an amine analog of TMB (2,4,6-trimethylpyridine, TMPy) prior to BA charge (section 2.7). TMPy is also too large to access the MFI channels and thus selectively titrates accessible surface protons. Titrated nMFI yielded no TM2B production after 2 h, but DBE formation was still observed, indicating that BA self-etherification occurred within MFI micropores and diffusion of BA and DBE (of similar d_{vdW} = 0.58 nm) was not entirely prohibited. In contrast, the larger size of TMB entirely prevented its diffusion into MFI micropores, in agreement with the literature.[10]

For MOR, it was hypothesized that neither BA nor TMB would access the 8-MR side pockets, thereby relegating all BA conversion to the unidimensional 12-MR channels. The

Table 2 ΔE_{disp} calculated for adsorbed BA, TMB, DBE, and TM2B in MFI, MOR, and BEA (eqn (2))

	ΔE_{disp} (kJ mol^{-1})			
Framework	BA	TMB	DBE	TM2B
MFI	−101	−163	−203	−263
BEA	−59	−78	−136	−155
MOR	−75	−104	−131	−170

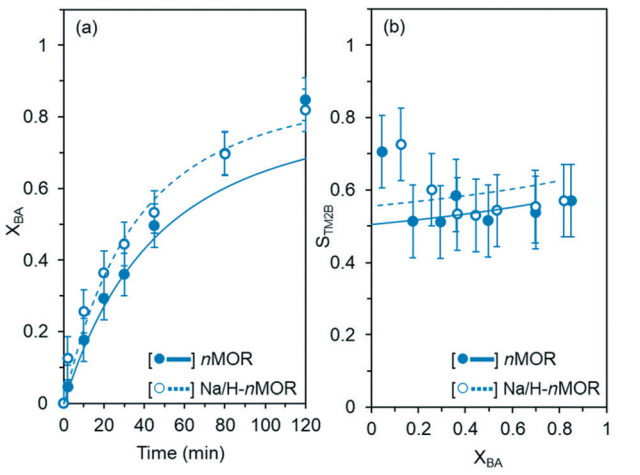

Fig. 4 (a) Fitted temporal X_{BA} (b) and S_{TM2B} for parent and partially Na-exchanged (35%) nMOR (neat, $[TMB]_0 : [BA]_0$ = 35 : 1, 393 K). Dashed and smooth curves correspond to model fits.

protons in the 8-MR were selectively ion-exchanged with Na^+ to yield Na/H-nMOR (with proton counts verified by NH_3-TPD), following published methods reporting that up to 55% of protons were located in 8-MR side pockets.[25] BA conversion and TM2B selectivity profiles were identical within 95% confidence for Na/H-nMOR relative to nMOR (Fig. 4), consistent with the protons located within 8-MR pockets being inaccessible for TMB alkylation and BA self-etherification.

3.2 Synthesis of hierarchical zeolites

Table 3 lists the suite of catalysts with measured Si/Al, proton densities ($[H^+]/g_{cat}$), proxy for extra-framework aluminum (H^+/Al), crystal diameters ($d_{crystal}$), BET surface areas (S_{BET}), micropore volumes (V_{micro}), and mesopore volumes (V_{meso}). Initial assessment of the textural properties shows that all post-synthetic treatments increased V_{meso} substantially and reduced Si/Al of hierarchical zeolites relative to their microporous analogs, the latter due to leached Si *via* desilication in aqueous NaOH either at ambient pressure (conventional desilication) or high pressure (recrystallization). High-pressure recrystallization is needed for successful mesopore formation in BEA because its polymorphic structure is otherwise too sensitive for conventional basic leaching at ambient pressure.[67] Recrystallization facilitates dissolution of the aluminosilicate backbone under high temperatures and pressures and the subsequent partial reformation of the dissolved backbone around mesoporous voids. SEM (Fig. S1†) shows that recrystallization yielded similarly sized crystals, suggesting the formation of internal mesopores. Observed conservation of crystal size (Fig. S2†) during recrystallization in aqueous NaOH is consistent with previously reported pseudomorphic interzeolite transformations (*i.e.*, from BEA to MFI), whereby crystal volume is conserved during internal mesopore-mediated restructuring of native micropore architecture.[68] Recrystallization also yielded larger mesopores in nBEA-h and μBEA-h compared to the mesopores in nMOR-h, μMOR-h, nMFI-h1, and nMFI-h2 produced through conventional desilication (Fig. 5). Conventional desilication is constrained to brief (≤30 min) ambient pressure conditions at mild temperatures because more severe times, temperatures, or [NaOH] reportedly cause excessive crystallinity losses and/or framework collapse.[40] In contrast, recrystallization enables more severe initial dissolution to generate larger voids because subsequent reformation of the tetrahedral aluminosilicate backbone around large mesopores re-stabilizes the overall framework.

nMOR and μMOR required dealumination pretreatments in HNO_3 prior to conventional desilication to increase Si/Al to within the optimal desilication range (Si/Al = 25–50), in agreement with published findings that zeolites with Si/Al < 25 contain excessively high [Al] that protect Si from desilication.[40] S_{BET} increased for nMOR-h (610 $m^2\ g^{-1}$) relative to nMOR (320 $m^2\ g^{-1}$) and decreased for μMOR-h (180 $m^2\ g^{-1}$) relative to μMOR (300 $m^2\ g^{-1}$), consistent with reduction in micropore volume for the latter (ΔV_{micro} = −84%), especially when compared to the insignificant change in V_{micro} for the former (ΔV_{micro} = +4%). ΔV_{meso} presumably varied due to different dealumination pretreatments (section 2.2) necessary to shift nMOR and μMOR into Si/Al = 25–50, where μMOR required more severe dealumination (6 M HNO_3, 2 h) than nMOR (2 M HNO_3, 4 h) due to the lower Si/Al of the former (Si/Al = 10 and 7.7 for nMOR and μMOR, respectively). nMFI, with Si/Al = 26, responded well to desilication without pretreatments, with V_{meso} increasing for longer desilication times in agreement with literature.[69,70] Extending desilication time from 15 min (for nMFI-h2) to 30 min (nMFI-h1) resulted in higher V_{meso} for the latter (0.34 and 0.32 $cm^3\ g^{-1}$ for nMFI-h1 and nMFI-h2, respectively) and negligible change in V_{micro} (0.033 and 0.031 $cm^3\ g^{-1}$ for nMFI-h1 and nMFI-h2, respectively). S_{BET} increased for desilicated MFI because small mesopores (Fig. 5) were formed *via* conventional desilication, and external surface area was greatly reduced, thereby exposing a greater fraction of micropores and small mesopores. Reduction of S_{BET} upon nBEA and μBEA recrystallization, by 18% and 1.8%, respectively, suggested destruction of high-surface area micropores and formation of lower-surface area

Table 3 Suite of synthesized and commercially sourced aluminosilicates

Catalyst	Source	Si/Al[a]	H^+/g_{cat}[b]	H^+/Al[b]	$d_{crystal}$[c]	S_{BET}[d]	V_{micro}[d,e] (% Δ)	V_{meso}[d,e] (% Δ)
Al-MCM-41	34	13	0.30	0.31	10	1500	≪1	0.81
nBEA	28–31	13	1.42	0.64	0.2	770	0.18	0.30
μ*B*EA	28–31	16	1.36	0.66	0.9	570	0.18	0.12
nBEA-h	23, 28–31	11	1.11	0.49	0.2	630	0.11 (−39)	0.48 (+60)
μBEA-h	23, 28–31	11	0.91	0.46	0.9	560	0.13 (−28)	0.35 (+190)
nMOR	Zeolyst	10	1.34	0.61	0.1	320	0.078	0.14
μMOR	33	7.7	1.40	0.58	20	300	0.092	0.090
nMOR-h	41, 43, 44	17	0.79	0.73	0.1	610	0.081 (+4)	0.39 (+180)
μMOR-h	33, 41, 43, 44	9.1	0.67	0.52	20	180	0.015 (−84)	0.12 (+33)
nMFI	26, 27	26	0.58	0.57	0.2	400	0.067	0.21
nMFI-h1	26, 27, 69	19	0.64	0.64	0.2	470	0.033 (−51)	0.34 (+62)
nMFI-h2	26, 27, 69	24	0.58	0.65	0.2	460	0.031 (−54)	0.32 (+52)

[a] EDXS. [b] NH_3-TPD (H^+/g_{cat} [=] mmol g^{-1}). [c] SEM (μm). [d] N_2 physisorption (S_{BET} [=] $m^2\ g^{-1}$, V [=] $cm^3\ g^{-1}$). [e] Relative to parent.

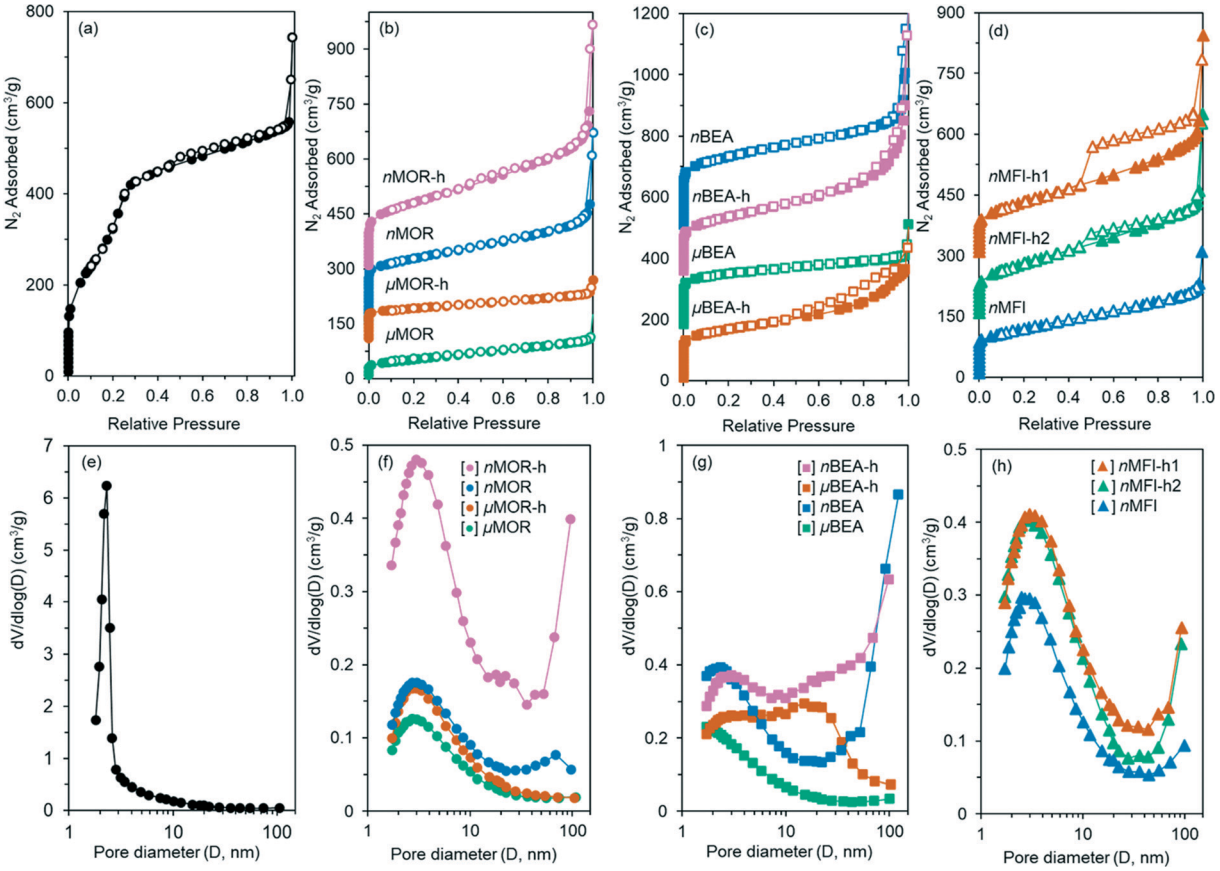

Fig. 5 N_2 physisorption isotherms for (a) Al-MCM-41, (b) MOR [*y*-shifts ($cm^3\ g^{-1}$): nMOR-h = +300; nMOR = +150; μMOR-h = +100], (c) BEA [*y*-shifts ($cm^3\ g^{-1}$): nBEA = +500; nBEA-h +350; μBEA = +175], and (d) MFI [*y*-shifts ($cm^3\ g^{-1}$): nMFI-h2 = +150; nMFI-h1= +300]; BJH pore size distributions for (e) Al-MCM-41, (f) MOR, (g) BEA, (h) MFI.

mesopores (positive ΔV_{meso}). However, ΔV_{meso} was greater for μBEA-h for the same recrystallization conditions (0.2 M NaOH, 21 h, 150 °C) used for nBEA-h, most likely due to differing composition of the parents, such as differing Si/Al or polymorph ratios.

The hierarchical zeolites largely retained the framework architectures and crystal morphologies of the microporous zeolites, as respectively confirmed by XRD (Fig. 6) and SEM (Fig. S1†). Desilication generally resulted in depression of diffraction intensities (*I*) for hierarchical zeolites relative to

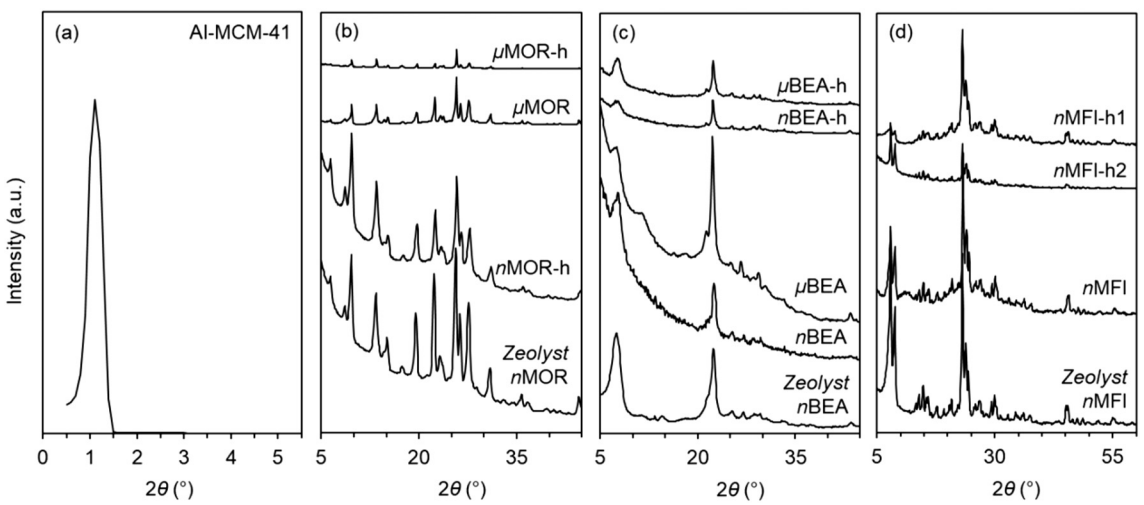

Fig. 6 Stacked XRD patterns for (a) Al-MCM-41, (b) MOR, (c) BEA (adjusted intensities = Zeolyst × 0.5; nBEA × 5; μBEA × 0.2), and (d) MFI.

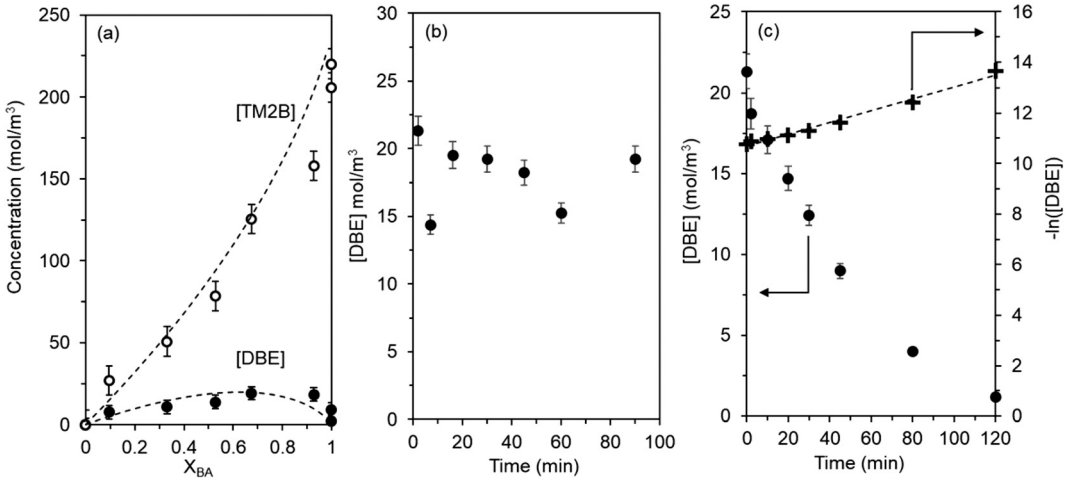

Fig. 7 (a) Fitted temporal [DBE] and [TM2B] for Al-MCM-41 (neat, $[TMB]_0 : [BA]_0 = 35 : 1$, 393 K). (b) Temporal [DBE] in absence of BA and TMB (Al-MCM-41, 393 K, $[DBE]_0$ = 21 mol m^{-3} in *n*-octane). (c) Temporal [DBE] (●) and fitted (dashed lines) pseudo first-order reaction of DBE to form TM2B (+, Al-MCM-41, 393 K, $[TMB]_0 : [DBE]_0 = 334 : 1$). Dashed lines correspond to model fits.

their microporous analogs because nonuniform mesopore formation results in loss of long-range crystallinity due to intervening voids that disrupt uniform framework periodicity. Changes in relative *I* at varying degrees of desilication within individual patterns yield insight into how these mesopores alter characteristic unit cells. For example, $I_{23^\circ} = 1.7 \times I_{8^\circ}$, $1.0 \times I_{8^\circ}$, and $3.5 \times I_{8^\circ}$ on nMFI, nMFI-h2, and nMFI-h1, respectively. Nonuniform change in I_{8° and I_{23° with increasing desilication time indicates nonuniform desilication of (−1 0 1) and (0 5 1) crystal facets, respectively,[60] in agreement with general lack of control over desilication. Some measure of bulk desilication control has been reported for Al-zoned MFI, which directs mesopore formation to Si-rich regions due to the ability of Al to serve as a protecting group against leaching of nearby Si.[38,70] However, all zeolite samples in this study contain uniformly distributed Al (as confirmed by EDXS) that cannot yield control over mesopore distribution.

3.3 Extraction of competitive rate constants from expanded reaction network

Temporal S_{TM2B} profiles were deconstructed to deduce the separate contributions of temporal [TM2B] and [DBE]. Both [TM2B] and [DBE] increased with time on all microporous, nanocrystalline zeolites. However, Al-MCM-41 and nMOR-h gave maximum values of [DBE], with re-consumption of [DBE] occurring at $[BA]/[DBE] < 0.1$ (Fig. 7a), which corresponds to $X_{BA} > 0.9$ for $[BA]_0 = 0.21 \times 10^{-3}$ mM. DBE re-consumption was accompanied by a non-monotonic increase in [TM2B]. Two potential secondary reactions included DBE cleavage to yield additional reactant BA and water or TM2B formation directly from DBE and TMB. The former was found to be insignificant at 393 K when DBE was charged in *n*-octane without TMB or BA (Fig. 7b). However, pseudo first-order TM2B production from DBE and TMB in the absence of BA was observed (Fig. 7c). While none of the microporous, nanocrystalline zeolites enabled this pathway in this work because they maintained $[BA]/[DBE] > 0.1$ for the reaction conditions studied here, the pathway was incorporated in data fitting for the hierarchical analogs as rates approached those of Al-MCM-41.

Following deduction of secondary TM2B formation from DBE, a more complete reaction network (Fig. 8) was built to describe all potential competing reaction pathways.

A system of ODEs modeling the reaction network, which assumed vacant protons dominated catalyst surfaces and included second-order exponential decay (eqn (5)–(7)),[71] agreed well with experimental concentration data (section S.4†). Deactivation accounted for pore blockage or site poisoning and was qualitatively supported by progressive catalyst discoloration from white to fuchsia (MOR) or brown (MFI, BEA, Al-MCM-41) during reaction. The TMB concentration here was nearly constant ($[TMB] \approx [TMB]_0$) because excess TMB was a solvent for this neat reaction:

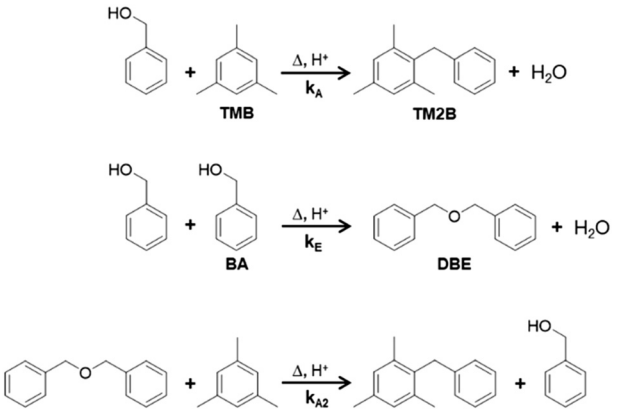

Fig. 8 Complete reaction scheme, including TMB alkylation, BA self-etherification, and secondary production of TM2B from DBE and TMB.

$$\frac{-r_{BA}}{[H^+]} = \left(k_A K_{BA}[TMB][BA] + k_E K_{BA}[BA]^{\beta} - k_{A2} K_{DBE}[TMB][DBE]\right) e^{-k_d t} \quad (5)$$

$$\frac{r_{TM2B}}{[H^+]} = (k_A K_{BA}[TMB][BA] + k_{A2} K_{DBE}[TMB][DBE]) e^{-k_d t} \quad (6)$$

$$\frac{r_{DBE}}{[H^+]} = \left(k_E K_{BA}[BA]^{\beta} - k_{A2} K_{DBE}[TMB][DBE]\right) e^{-k_d t} \quad (7)$$

Another model, which discounted the deactivation term and included both BA and vacant protons as abundant surface adsorbates, did not agree as well with experimental data (section S.5†). The model used here was advantageous over a simple first-order tangential fit of low X_{BA} data (initial rates) because it enabled quantification of deactivation rate constants and because secondary reaction of DBE with TMB occurred only at $X_{BA} > 0.9$ at studied conditions.

Microporous zeolites were modeled with reduced reaction orders (β) equivalent to $\beta = (\alpha + 1)/2$, where $\alpha = 2$ and $\beta = 3/2$ for self-etherification or $\alpha = \beta = 1$ for pseudo first-order alkylation with respect to [BA].[72] Reduced orders are consistent with published accounts of severe diffusion constraints for this reaction system in microporous BEA and MFI,[10,21–23] as well as DFT-calculated van der Waals diameters (d_{vdW}) of TMB, TM2B, and DBE relative to pore-limiting diameters of zeolite micropores (Fig. 3 and S3†). Fits for microporous, nanocrystalline catalysts were included in Fig. 2, as well as for the full catalyst suite in Fig. 9. The fitted temporal X_{BA} and S_{TM2B} show that all nanocrystalline zeolites, both microporous and hierarchical, achieved final X_{BA} greater than their microcrystalline counterparts after 2 h. The proton density-normalized initial and cumulative rates for all catalysts are listed in Table 4. Initial rates decreased with increasing crystal size of a given framework, consistent with the longer time necessary for diffusing reactants to reach protons at crystal centers. Only nMOR-h yielded a

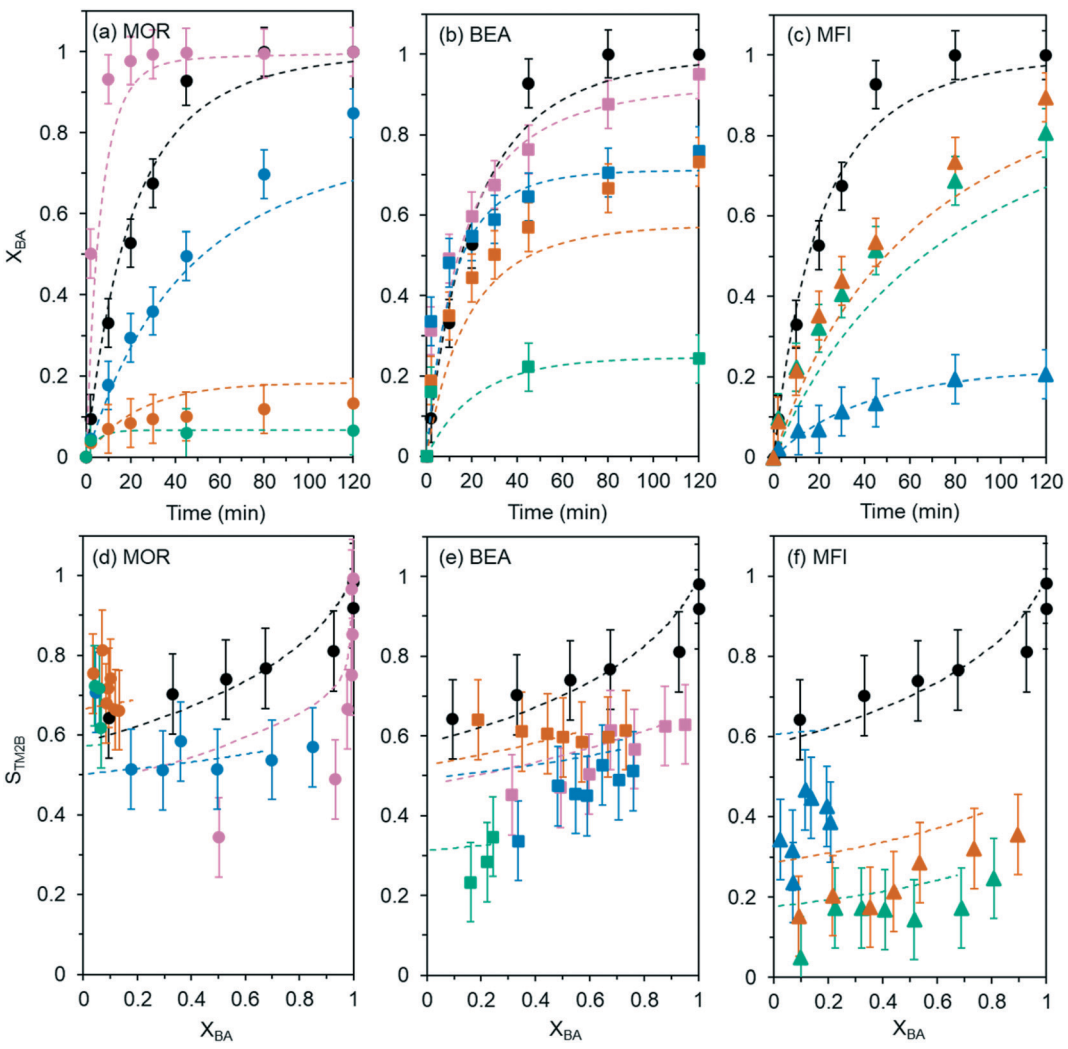

Fig. 9 Fitted temporal X_{BA} curves for Al-MCM-41 (●) and (a) MOR [nMOR (●), μMOR (●), nMOR-h (●), μMOR-h (●)], (b) BEA [nBEA (■), μBEA (■), nBEA-h (■), μBEA-h (■)], and (c) MFI [nMFI (▲), nMFI-h1 (▲), nMFI-h2 (▲)] with corresponding (d)–(f) fitted temporal S_{TM2B} curves (neat, $[TMB]_0$: $[BA]_0$ = 35 : 1, 393 K). Dashed lines correspond to model fits.

Table 4 Fitted rate constants normalized by total proton densities, as well as initial and cumulative consumption rates. Values in parenthesis are 95% confidence intervals

Catalyst	k_AK_{BA} [a]	k_EK_{BA} [a]	$k_{A2}K_{BA}$ [a]	k_d [b]	Rate [c] Initial	Rate [c] Cumulative
nMOR-h ●	6.2 (2.3)	110 (110)	1.3 (2.5)	0 (2.9)	860 (1)	48 (4)
Al-MCM-41 ●	2.5 (0.3)	30 (23)	0.73 (4.3)	0 (0.37)	340 (22)	57 (3)
nBEA-h ■	0.72 (0.13)	13 (8)	0	1.1 (0.4)	110 (1)	15 (2)
nBEA ■	0.62 (0.11)	0.39 (0.19)	0	2.9 (0.5)	90 (1)	9.2 (1.3)
μBEA-h ■	0.50 (0.11)	7.6 (5.3)	0	2.1 (0.6)	72 (1)	14 (4)
μMOR-h ●	0.44 (0.08)	3.7 (2.9)	0	2.4 (0.5)	55 (1)	7.5 (1.3)
nMOR ●	0.40 (0.07)	0.11 (0.05)	0	0.6 (0.2)	60 (1)	24 (7)
μMOR ●	0.32 (0.06)	0.057 (0.031)	0	12 (2)	40 (1)	1.8 (0.2)
nMFI-h1 ▲	0.23 (0.07)	9.7 (3.2)	0	0 (0.26)	53 (1)	24 (5)
nMFI ▲	0.15 (0.02)	0.023 (0.004)	0	1.3 (0.1)	20 (1)	6.2 (0.3)
nMFI-h2 ▲	0.14 (0.08)	11(4)	0	0 (0.36)	47 (1)	24 (7)
μBEA ■	0.083 (0.056)	0.061 (0.041)	0	2.4 (1.0)	17 (1)	3.1 (0.7)

[a] $[M^{-1}\ s^{-1}]$. [b] $[h^{-1}]$. [c] [mM-BAmin^{-1} mmol-H^{+-1}].

greater initial rate (860 mM-BA min^{-1} mmol-H^{+-1}) than Al-MCM-41 (340 mM-BA min^{-1} mmol-H^{+-1}), with both reaching complete conversion (X_{BA} = 1.0) within 2 h. The nanocrystalline, microporous zeolites (nMOR, nBEA) achieved greater cumulative rates (24 and 9.2 mM-BA min^{-1} mmol-H^{+-1}, respectively) than their microcrystalline, microporous counterparts (μMOR and μBEA with 1.8 and 3.1 mM-BA min^{-1} mmol-H^{+-1}, respectively), where the decrease in rate was exacerbated in the large 1D crystal (μMOR). Unlike initial rates, which correlated positively with V_{meso} and negatively with $d_{crystal}$ for a given framework, S_{TM2B} at equivalent X_{BA} did not correlate uniformly with V_{meso} or $d_{crystal}$ across all zeolite architectures. For example, nMFI gave higher S_{TM2B} than nMFI-h1 and nMFI-h2 for all equivalent X_{BA}, whereas μBEA gave lower S_{TM2B} than μBEA-h at all equivalent X_{BA}. Thus, observed lumped rate constants for alkylation (k_AK_{BA}), etherification (k_EK_{BA}), secondary TM2B formation from DBE ($k_{A2}K_{BA}$) and deactivation (k_d) were extracted from fits to decouple effects of deactivation and reaction. The rate constants in Table 4 correlate to the observed values, which may reflect internal diffusion limitations particularly for the microporous zeolites. Note that the proton-normalized observed lumped rate constants for alkylation and self-etherification (k_AK_{BA} and k_EK_{BA}, respectively) for nMOR, μMOR, nMOR-h, and μMOR-h were normalized by 45% of the total proton count, corresponding to protons within 12-MR channels. This assumption is weaker for nMOR-h and μMOR-h, which may have altered proton distributions due to the post-synthetic treatments.

In theory, k_AK_{BA} for protons within internal MFI micropores should be zero because TMB alkylation was only observed to occur on surface protons. Consequently, the small fitted k_AK_{BA} in Table 4 arises from surface protons (reportedly less than 3% of total protons on MFI)[22] and protons near pore mouths. If the alkylation rate on nMFI was normalized by surface proton density, then the subsequent k_AK_{BA} would be of similar order to that of Al-MCM-41. Therefore, mesopores behave analogously to crystal surfaces with respect to the lack of molecule confinement. The k_AK_{BA} and k_EK_{BA} trends of nMFI < nMOR < nBEA in Table 4 agree with expected structure–function behaviors as diffusion in MFI micropores is essentially impossible for TMB and severely hindered for BA. MOR has a larger channel size than BEA (PLD = 0.65 nm and 0.60 nm, respectively),[62,64] but the 3D network of BEA enables more diffusional pathways, compared to 1D MOR, to circumvent carbonaceous blockages or otherwise host higher concentrations of TM2B and DBE precursors. The 3D BEA architecture yielded higher observed alkylation and etherification rates than the 1D MOR architecture, with nBEA giving k_AK_{BA} = 0.62 ± 0.11 $M^{-1}\ s^{-1}$ and k_EK_{BA} = 0.39 ± 0.19 $M^{-1}\ s^{-1}$ and nMOR giving k_AK_{BA} = 0.40 ± 0.07 $M^{-1}\ s^{-1}$ and k_EK_{BA} = 0.11 ± 0.05 $M^{-1}\ s^{-1}$. Simultaneously, the deactivation rate constant (k_d) is nearly five times greater on nBEA than nMOR (k_d = 2.9 ± 0.5 h^{-1} and 0.6 ± 0.2 h^{-1}, respectively) because the enhanced TMB accommodation in nBEA over nMOR may result in faster deactivation. The k_d for nMFI (1.3 ± 0.1 h^{-1}) is about half that of nBEA, owing to the inaccessibility of TMB altogether; as such, we expect that nMFI deactivation species likely form primarily from DBE precursors. Because TMB alkylation occurs exclusively on surface protons, S_{TM2B} on nMFI is comparable to that of nBEA for all X_{BA} (Fig. 9) despite nMFI achieving X_{BA} three to four times lower than nBEA after 2 h of reaction.

Structure–function relationships for microporous zeolites associated with crystal size are deduced through comparison of the observed rate constants in Table 4 for nBEA with μBEA and nMOR with μMOR. k_AK_{BA} and k_EK_{BA} decreased with increasing crystal size for both architectures, in agreement with subdued internal diffusion owing to extended diffusion path lengths. Deactivation rates increased more significantly for μMOR over nMOR than for μBEA over nBEA, owing to the much larger crystal size difference for the MOR samples. Further, the 1D network in MOR renders guest moieties exclusively dependent on a single diffusion path that, once occluded, cannot be circumvented by connecting pathways as

within the 3D BEA network. Crystal size effects were not considered for the MFI architecture because the 10-MR channels in MFI already prohibit TMB alkylation on protons within micropores, regardless of crystal size.

k_AK_{BA} and k_EK_{BA} increased for the respective hierarchical analogs of all tested zeolites, manifesting in steeper BA conversion (X_{BA}) curves (Fig. 9) due to higher initial rates. Notably, nMOR-h yielded k_AK_{BA} and k_EK_{BA} values even greater than those for the Al-MCM-41 control, consistent with combined effects of mitigation of diffusional limitations and preferential van der Waals solvation of reaction moieties in pores of proper molecular dimension. However, higher S_{TM2B} on Al-MCM-41 than on nMOR-h at all $X_{BA} < 0.9$ indicates that DBE formation preferentially occurs in micropores, consistent with DFT-calculated dispersive energy trends (Table 2). S_{TM2B} converges for Al-MCM-41 and nMOR-h when [BA]/[DBE] < 0.1 (Fig. 9) due to consumption of DBE to form TM2B, such that sole consideration of the product distributions and final X_{BA} at 2 h for these two catalysts renders them indistinguishable. Both give $k_d \sim 0$, indicating that deactivation time scales exceed the time to reach reaction completion at studied BA concentrations. Hierarchical zeolites yield final reaction outcomes comparable to mesoporous aluminosilicates like Al-MCM-41. The combination of small crystal size (smaller even than nBEA-h), high V_{meso} to mitigate fouling,[73] large micropores, and high acid site density (Table 4) relative to the other microporous and hierarchical zeolites all contributed to low R^2/D_e that enabled high BA conversion for nMOR-h.

Reaction outcomes for BEA show a compensatory effect whereby μBEA-h gave similar X_{BA} and S_{TM2B} profiles to nBEA (Fig. 9b and e). Enhanced diffusivity of DBE and TM2B precursors in μBEA-h appears to compensate for the >4× larger crystal diameter of μBEA compared to nBEA. μBEA-h also gave higher k_EK_{BA} than nBEA, and similar k_AK_{BA}. For MOR, the compensatory effect of mesopores within the context of crystal size similarly manifests in higher k_EK_{BA} and k_AK_{BA} for μMOR-h than nMOR, but the drastically subdued cumulative rate for μMOR-h relative to nMOR (respectively 7.5 and 24 mM-BA min^{-1} $mmol\text{-}H^{+-1}$) arises from the high k_d of μMOR-h, owing to its massive size ($d_{crystal}$ = 20 μm). The $\Delta d_{crystal}$ between nMOR and μMOR (or μMOR-h) far exceeds that of nBEA and μBEA (or μBEA-h), suggesting that mesopores are limited in the extent to which they can alleviate the internal diffusion constraints imposed by high crystal diameters. High crystal radii must be sufficiently compensated by high D_e that drives down R^2/D_e to achieve $\phi \leq 1$, corresponding to kinetically controlled catalysis. For μMOR with exceptionally large $d_{crystal}$ = 20 μm, higher V_{meso} and greater mesopore–micropore connectivity is required to achieve the same net diffusional enhancement that μBEA-h provides over μBEA, which is much smaller ($d_{crystal}$ = 900 nm). In this case, S_{TM2B} is greater on μMOR-h than nMOR at all equivalent X_{BA}, suggesting that alkylation occurs primarily on surface or sub-surface protons due to rapid deactivation of internal micropores in the large crystal.

Mesopores appear to enhance access to internal protons otherwise confined within prohibitively narrow micropores in nMFI. nMFI-h1 and nMFI-h2 give similar X_{BA} and S_{TM2B} profiles (Fig. 9c and f), a quadrupled X_{BA} after 2 h relative to nMFI but also showing that S_{TM2B} decreases relative to nMFI for all equivalent X_{BA}. Desilication leached portions of the crystal, resulting in a redistribution of protons that increased the fraction of protons accessible only to DBE and BA, as S_{TM2B} values remained low. As with nMOR-h, the nMFI-h1 and nMFI-h2 gave $k_d \sim 0$ indicating that mesopores mitigated fouling.[73] Higher k_d on nBEA-h than on nMFI-h1 and nMFI-h2 may result from the significantly higher k_AK_{BA} and k_EK_{BA} for nBEA-h, such that higher rates of alkylation and etherification reduces the deactivation time scale owing to rapid buildup of fouling precursors.

We further postulate that deactivation primarily originated from poor diffusion of TMB, consistent with qualitatively observed discoloration of catalyst in TMB at 363 K (section 2.4) prior to BA addition. TMB existed in 35-fold molar excess, therefore carbon balances for alkylation and etherification calculated on a BA basis are minimally impacted by fouling. All carbon balances were calculated to be ≥88% at 120 min, and 7 of the 12 studied catalysts gave carbon balances >95%. Sub-100% carbon balances should not impact conclusions drawn from presented selectivities (Fig. 9), which indicate ratios of products.

3.4 Effects of solvation environment in hierarchical zeolites on diffusion-corrected rate constants and subsequent diffusivity enhancements

Not all the extracted observed rate constants for microporous zeolites (Table 4) reflect intrinsic kinetics; rather, they may include significant artifacts of diffusion, as is the case for many microporous catalysts with reactions of bulky molecules. Therefore, available TMB diffusivity data[61–65] were used to calculate corrected alkylation rate constants, $(k_AK_{BA})_{corrected}$, for nBEA, μBEA, nMOR, and μMOR according to derived relationships between observed and intrinsic rate constants at high Thiele moduli:[72]

$$(k_AK_{BA})_{corrected} = \frac{\rho_{H^+}R^2}{D_e}\left[\frac{k_AK_{BA}}{3}\right]^2 \quad (8)$$

Reliable diffusivity data for DBE were not available, but this same approach would be theoretically relevant for reaction–diffusion analysis of BA self-etherification. Regardless, TMB alkylation analysis yields insight into the most dramatic shifts in D_e, owing to the larger d_{vdW} of TMB than DBE. For nMFI, we assumed that $(k_AK_{BA})_{corrected} = k_AK_{BA}$ given that alkylation occurred only on surface protons. D_e values were unavailable for hierarchical zeolites and are expected to have a nuanced dependence on micropore–mesopore connectivity for each catalyst.[24] Therefore, D_e were calculated for $\phi = 1.0$ to deduce whether the minimum D_e necessary for each hierarchical zeolite to reach the kinetically controlled alkylation regime, such that $(k_AK_{BA})_{corrected} = k_AK_{BA}$, was

Table 5 $(k_AK_{BA})_{corrected}$ and D_e for studied catalysts. Values in parenthesis are 95% confidence intervals

Catalyst	$(k_AK_{BA})_{corrected}$ [a]	D_e [b] ($\times 10^{10}$)
nMOR-h ●	7.4 (2.8)	0.16
Al-MCM-41 ●	3.0 (0.3)	310
nBEA-h ■	0.87 (0.16)	0.18
nBEA ■	39 (15)	0.0046[c]
μBEA-h ■	0.61 (0.14)	2.6
μMOR-h ●	0.53 (0.10)	1300
nMOR ●	0.92 (0.35)	0.019[c]
μMOR ●	29 000 (13 000)	0.019[c]
nMFI-h1 ▲	0.28 (0.08)	0.05
nMFI ▲	0.17 (0.01)	0.000071[c]
nMFI-h2 ▲	0.17 (0.09)	0.030
μBEA ■	22 (39)	0.0046[c]

[a] (M^{-1} s^{-1}). [b] (cm^2 s^{-1}). [c] Estimated from literature.

feasible relative to reported increases in D_e in hierarchical zeolites for diffusion of other substituted aromatics like toluene and cumene:[72,74]

$$\phi = 1.0 = \frac{R}{3}\left[\frac{k_AK_{BA}\rho_{H^+}}{D_e}\right]^{1/2} \quad (9)$$

Calculated and/or reported diffusivities and $(k_AK_{BA})_{corrected}$ are listed in Table 5. Zeolites differing only in nominal crystal size (*i.e.*, nBEA *versus* μBEA) have similar internal structures; therefore, solvation around a given proton should be similar and manifest in similar intrinsic rate constants when internal diffusion has been corrected for utilizing eqn (8) and (9). However, only nBEA and μBEA yielded similar $(k_AK_{BA})_{corrected}$ values within a 95% confidence interval. The assumption breaks down if a zeolite framework contains multiple solvation environments, or if synthesis protocols to yield different crystal sizes also result in different proton distributions. The correction is not sufficient to converge rate constants for nMOR and μMOR, because the Thiele modulus correction does not account for changes in selectivity owing to protons in different solvation environments (*i.e.*, surface protons *versus* protons in 12-MR channels, as protons in 8-MR channels are inaccessible to alkylation or etherification as previously described). Exceptionally high $(k_AK_{BA})_{corrected}$ for μMOR likely results from alkylation on surface or sub-surface protons, considering that the massive k_d (Table 4) suggests rapid inactivation of internal protons owing to severe internal diffusion constraints resulting from μMOR's large size ($d_{crystal}$ = 20 μm). Surface protons enable high TM2B selectivity due to the absence of prohibitively narrow confining voids otherwise enclosing internal protons.

D_e effects on Thiele moduli for BEA (Fig. S9†) show how pore architecture impacts kinetic *versus* diffusion control of reaction systems. If the hierarchical systems have protons located within mesopores, they will possess solvation environments different from their microporous analogs, resulting in different intrinsic reaction rate constants. Even if protons are not located within mesopores, D_e still differs between hierarchical and microporous zeolites because the larger pores in the former impact ingress/egress of reaction moieties. Relative to the D_e for TMB in nBEA estimated from the literature,[61,63,65] nBEA-h and μBEA-h must respectively increase D_e by 39× or 560× in order for $(k_AK_{BA})_{corrected} = k_AK_{BA}$ to give $\phi \leq 1.0$. For nMFI-h2 and nMFI-h1, D_e must respectively increase by at least 430× or 760×, while for nMOR-h and μMOR-h D_e must increase by 8× and 68 000×, respectively. All of these increases are feasible within the contexts of previous diffusivity improvements,[74] except μMOR-h which would require further increases in V_{meso} to fully compensate for its large crystal size, as previously discussed. All of these calculated D_e requirements are in agreement with published increases in mass diffusivity of aromatic molecules for hierarchical MFI produced *via* a variety of methods, including conventional desilication.[74]

Agreement with published diffusivity improvements supports the initial assumption that all hierarchical zeolites studied here likely operate under kinetically controlled regimes. This assumption is slightly weaker for μMOR-h because of the high R^2/D_e of μMOR, which necessitates a drastic improvement in TMB diffusivity. These D_e increases all correlate with mesopore efficacy, which we define here as the ability of mesopores to increase conversion of bulky reactants and/or enhance selectivity to bulky products otherwise excluded from, or poorly solvated within, prohibitively narrow zeolite micropores. By extension, increases in conversion and selectivity for relatively bulky reaction moieties necessitates reduction of deactivation rates. Assuming constant crystal size, the extent to which the Thiele modulus can be reduced is dictated by total V_{meso}, micropore–mesopore connectivity, and proton distribution in mesopores relative to micropores. These crucial factors depend greatly on the method of mesopore formation,[20,39] three of which we explored here: (1) high-pressure basic recrystallization for BEA, (2) ambient pressure basic desilication for MFI, and (3) ambient pressure basic desilication for MOR following a dealumination pretreatment in acid. While clear differences in subsequent mesopore distribution arose among these techniques (*i.e.*, larger mesopores in nBEA-h and μBEA-h were formed *via* recrystallization than either ambient pressure desilication technique), the uniformly feasible increases in D_e calculated from the extracted rate constants for all hierarchical zeolites here point to the versatility of post-synthetic mesopore formation.

4 Conclusions

This work illustrates the importance of contextualizing mesopore efficacy in hierarchical zeolites according to crystal size, microporous architecture of zeolite parent frameworks, and proton distributions. For complex reaction networks involving bulky molecules, such as the probe alkylation of TMB with BA presented here, we show that hierarchical zeolites could achieve similar conversions and selectivities to

bulky products as purely mesoporous aluminosilicates (Al-MCM-41), whereas the microporous zeolites could not. Initial and cumulative reaction rates are interpreted by alkylation, etherification, and deactivation rate constants extracted from a detailed reaction network model that accounts for secondary formation of TM2B from DBE and TMB, a route for product control that has been previously de-emphasized at the expense of understanding nuanced structure–function relations of hierarchical zeolites. DFT-calculated dispersive energy changes (ΔE_{disp}) for BA, TMB, DBE, and TM2B adsorption in microporous zeolites are consistent with observed alkylation rates, which increase with nMFI < nMOR < nBEA in parallel with decreasing $|\Delta E_{disp}|$ that reflect increasingly facile solvation of reaction moieties within (intersecting) voids of increasing size. These baseline solvation interactions within microporous architectures yield insight into subsequent mesopore effects in hierarchical zeolites, for which we estimate the minimum diffusivity improvements, relative to respective microporous parents, necessary to achieve kinetic control. All the studied post-synthetic mesopore incorporation techniques (ambient pressure desilication, ambient pressure desilication preceded by acidic dealumination, and basic recrystallization) yielded kinetically controlled catalysts, thus reflecting the versatility of hierarchical zeolites for facilitating otherwise extremely diffusion limited reactions of poly-substituted aromatics in the liquid phase.

Conflicts of interest

There are no conflicts of interest to declare.

Acknowledgements

The authors acknowledge support from the High Meadows Environmental Institute at Princeton University, and the use of the Princeton University NMR Facility. The authors also acknowledge the use of Princeton's Imaging and Analysis Center, which is partially supported through the Princeton Center for Complex Materials (PCCM), a National Science Foundation (NSF)-MRSEC program (DMR-2011750). The authors also acknowledge Professor David Hibbitts at the University of Florida for providing access to, and training for, DFT computations through the Computational Catalysis Interface (CCI).[51]

References

1 R. Gounder and E. Iglesia, *Chem. Commun.*, 2013, **49**, 3491–3509.
2 K. Li, J. Valla and J. Garcia-Martinez, *ChemCatChem*, 2014, **6**, 46–66.
3 R. G. Grim, A. T. To, C. A. Farberow, J. E. Hensley, D. A. Ruddy and J. A. Schaidle, *ACS Catal.*, 2019, **9**, 4145–4172.
4 M. L. Sarazen and E. Iglesia, *ChemCatChem*, 2018, **10**, 4028–4037.
5 M. L. Sarazen, E. Doskocil and E. Iglesia, *ACS Catal.*, 2016, **6**, 7059–7070.
6 J. Q. Bond, A. A. Upadhye, H. Olcay, G. A. Tompsett, J. Jae, R. Xing, D. M. Alonso, D. Wang, T. Zhang, R. Kumar, A. Foster, S. M. Sen, C. T. Maravelias, R. Malina, S. R. H. Barrett, R. Lobo, C. E. Wyman, J. A. Dumesic and G. W. Huber, *Energy Environ. Sci.*, 2014, **7**, 1500–1523.
7 Q. Almas, C. Sievers and C. W. Jones, *Appl. Catal., A*, 2019, **571**, 107–117.
8 S. Bhatia, J. Beltramini and D. D. Do, *Catal. Rev.: Sci. Eng.*, 1989, **31**, 431–480.
9 C. H. Bartholomew, *Appl. Catal., A*, 2001, **212**, 17–60.
10 X. Zhang, D. Liu, D. Xu, S. Asahina, K. A. Cychosz, K. V. Agrawal, Y. Al Wahedi, A. Bhan, S. Al Hashimi, O. Terasaki, M. Thommes, M. Tsapatsis, M. Thommes and M. Tsapatsis, *Science*, 2012, **336**, 1684–1687.
11 A. Korde, B. Min, Q. Almas, Y. Chiang, S. Nair and C. W. Jones, *ChemCatChem*, 2019, **11**, 4548–4557.
12 W. J. Roth and J. Ejka, *Catal. Sci. Technol.*, 2011, **1**, 43–53.
13 M. R. Whitaker, A. Parulkar and N. A. Brunelli, *Mol. Syst. Des. Eng.*, 2020, **5**, 257–268.
14 M. J. Climent, A. Corma, S. Iborra, S. Miquel, J. Primo and F. Rey, *J. Catal.*, 1999, **183**, 76–82.
15 C. T. Kresge, M. E. Leonowicz, W. J. Roth, J. C. Vartuli and J. S. Beck, *Nature*, 1992, **359**, 710–712.
16 D. T. On and S. Kaliaguine, *Angew. Chem., Int. Ed.*, 2002, **114**, 1078–1082.
17 M. Milina, S. Mitchell, P. Crivelli, D. Cooke and J. Pérez-Ramírez, *Nat. Commun.*, 2014, **5**, 3922.
18 J. A. Martens, D. Verboekend, K. Thomas, G. Vanbutsele, J. P. Gilson and J. Pérez-Ramírez, *ChemSusChem*, 2013, **6**, 421–425.
19 J. C. Groen, W. Zhu, S. Brouwer, S. J. Huynink, F. Kapteijn, J. A. Moulijn and J. Pérez-Ramírez, *J. Am. Chem. Soc.*, 2007, **129**, 355–360.
20 L. Forster, M. Lutecki, H. Fordsmand, L. Yu and C. D'Agostino, *Mol. Syst. Des. Eng.*, 2020, **5**, 1193–1204.
21 D. Liu, X. Zhang, A. Bhan and M. Tsapatsis, *Microporous Mesoporous Mater.*, 2014, **200**, 287–290.
22 D. Xu, O. Abdelrahman, S. H. Ahn, Y. Guefrachi, A. Kuznetsov, L. Ren, S. Hwang, M. Khaleel, S. Al Hassan, D. Liu, S. B. Hong, P. Dauenhauer and M. Tsapatsis, *AIChE J.*, 2019, **65**, 1067–1075.
23 K. Zhang, S. Fernandez, J. T. O'Brien, T. Pilyugina, S. Kobaslija and M. L. Ostraat, *Catal. Today*, 2018, **316**, 26–30.
24 F. Thibault-Starzyk, I. Stan, S. Abelló, A. Bonilla, K. Thomas, C. Fernandez, J. P. Gilson and J. Pérez-Ramírez, *J. Catal.*, 2009, **264**, 11–14.
25 R. Gounder and E. Iglesia, *J. Am. Chem. Soc.*, 2009, **131**, 1958–1971.
26 B. Gevert, L. Eriksson and A. Törncrona, *J. Porous Mater.*, 2011, **18**, 723–728.
27 T. Otto, S. I. Zones and E. Iglesia, *Microporous Mesoporous Mater.*, 2018, **270**, 10–23.
28 M. A. Camblor and J. Pérez-Pariente, *Zeolites*, 1991, **11**, 202–210.

29 M. A. Camblor, A. Corma and S. Valencia, *Microporous Mesoporous Mater.*, 1998, **25**, 59–74.
30 M. A. Camblor, A. Mifsud and J. Pérez-Pariente, *Zeolites*, 1991, **11**, 792–797.
31 Beta, in *Verified Syntheses of zeolitic materials*, ed. S. Mintova, 2016, p. 156.
32 M. A. Camblor, A. Corma, A. Mifsud, J. Pérez-Pariente and S. Valencia, *Stud. Surf. Sci. Catal.*, 1997, **105**, 341–348.
33 B. O. Hincapie, L. J. Garces, Q. Zhang, A. Sacco and S. L. Suib, *Microporous Mesoporous Mater.*, 2004, **67**, 19–26.
34 O. Franke, J. Starekb and A. Zukalb, *J. Chem. Soc., Chem. Commun.*, 1993, 1992–1994.
35 A. Chawla, R. Li, R. Jain, R. J. Clark, J. G. Sutjianto, J. C. Palmer and J. D. Rimer, *Mol. Syst. Des. Eng.*, 2018, **3**, 159–170.
36 A. J. Jones, S. I. Zones and E. Iglesia, *J. Phys. Chem. C*, 2014, **118**, 17787–17800.
37 J. C. Groen, L. A. A. Peffer, J. A. Moulijn and J. Pérez-Ramírez, *Colloids Surf., A*, 2004, **241**, 53–58.
38 J. C. Groen, L. A. A. Peffer, J. A. Moulijn and J. Pérez-Ramírez, *Chem. – Eur. J.*, 2005, **11**, 4983–4994.
39 D. Verboekend and J. Pérez-Ramírez, *Catal. Sci. Technol.*, 2011, **1**, 879–890.
40 J. C. Groen, J. A. Moulijn and J. Pérez-Ramírez, *J. Mater. Chem.*, 2006, **16**, 2121–2131.
41 J. C. Groen, T. Sano, J. A. Moulijn and J. Pérez-Ramírez, *J. Catal.*, 2007, **251**, 21–27.
42 J. C. Groen, L. A. A. Peffer, J. A. Moulijn and J. Pérez-Ramírez, *Microporous Mesoporous Mater.*, 2004, **69**, 29–34.
43 X. F. Li, R. Prins and J. A. van Bokhoven, *J. Catal.*, 2009, **262**, 257–265.
44 R. Giudici, H. W. Kouwenhoven and R. Prins, *Appl. Catal., A*, 2000, **203**, 101–110.
45 J. C. Groen, L. A. A. Peffer and J. Pérez-Ramírez, *Microporous Mesoporous Mater.*, 2003, **60**, 1–17.
46 M. Thommes, K. Kaneko, A. V. Neimark, J. P. Olivier, F. Rodriguez-Reinoso, J. Rouquerol and K. S. W. Sing, *Pure Appl. Chem.*, 2015, **87**, 1051–1069.
47 G. Kresse and J. Furthmüller, *Comput. Mater. Sci.*, 1996, **6**, 15–50.
48 G. Kresse and J. Furthmüller, *Phys. Rev. B*, 1996, **54**, 11169–11186.
49 G. Kresse and J. Hafner, *Phys. Rev. B*, 1993, **47**, 558–561.
50 G. Kresse and J. Hafner, *Phys. Rev. B*, 1994, **49**, 14251–14269.
51 P. Kravchenko, C. Plaisance and D. Hibbitts, *ChemRxiv*, 2019, DOI: 10.26434/chemrxiv.8040737.v3.
52 P. E. Blochl, *Phys. Rev. B*, 1994, **50**, 17953–17979.
53 G. Kresse and D. Joubert, *Phys. Rev. B: Condens. Matter Mater. Phys.*, 1999, **59**, 1758–1775.
54 B. Hammer, L. B. Hansen and J. K. Nørskov, *Phys. Rev. B: Condens. Matter Mater. Phys.*, 1999, **59**, 7413–7421.
55 J. P. Perdew, K. Burke and M. Ernzerhof, *Phys. Rev. Lett.*, 1996, **77**, 3865–3868.
56 Y. Zhang and W. Yang, *Phys. Rev. Lett.*, 1998, **80**, 890.
57 H. J. Monkhorst and J. D. Pack, *Phys. Rev. B: Solid State*, 1976, **13**, 5188–5192.
58 S. Grimme, S. Ehrlich and L. Goerigk, *J. Comput. Chem.*, 2011, **32**, 1456–1465.
59 S. Grimme, J. Antony, S. Ehrlich and H. Krieg, *J. Chem. Phys.*, 2010, **132**, 154104.
60 C. Baerlocher and L. B. McCusker, *Database of Zeolite Structures*.
61 G. Mirth, J. Čejka and J. A. Lercher, *J. Catal.*, 1993, **139**, 24–33.
62 J. Čejka, J. Kotrla and A. Krejčí, *Appl. Catal., A*, 2004, **277**, 191–199.
63 J. Xiao and J. Wei, *Chem. Eng. Sci.*, 1992, **47**, 1123–1141.
64 N. M. Tukur and S. Al-Khattaf, *Energy Fuels*, 2007, **21**, 2499–2508.
65 M. DeLuca and D. Hibbitts, *ChemRxiv*, 2019, DOI: 10.26434/chemrxiv.8035565.v1.
66 M. L. Sarazen, E. Doskocil and E. Iglesia, *J. Catal.*, 2016, **344**, 553–569.
67 J. C. Groen, S. Abelló, L. A. Villaescusa and J. Pérez-Ramírez, *Microporous Mesoporous Mater.*, 2008, **114**, 93–102.
68 S. Goel, S. I. Zones and E. Iglesia, *Chem. Mater.*, 2015, **27**, 2056–2066.
69 J. C. Groen, J. C. Jansen, J. A. Moulijn and J. Pérez-Ramírez, *J. Phys. Chem. B*, 2004, **108**, 13062–13065.
70 J. C. Groen, T. Bach, U. Ziese, A. M. Paulaime-Van Donk, K. P. De Jong, J. A. Moulijn and J. Pérez-Ramírez, *J. Am. Chem. Soc.*, 2005, **127**, 10792–10793.
71 H. S. Fogler, *Elements of Chemical Reaction Engineering*, Wiley, 2006.
72 M. E. Davis and R. E. Davis, *Fundamentals of Chemical Reaction Engineering*, McGraw-Hill, 2003.
73 K. Lee, S. Lee, Y. Jun and M. Choi, *J. Catal.*, 2017, **347**, 222–230.
74 L. Gueudré, M. Milina, S. Mitchell and J. Pérez-Ramírez, *Adv. Funct. Mater.*, 2014, **24**, 209–219.